

The transport dynamics of tens of micrometer-sized water droplets in RF atmospheric pressure glow discharges

Gaurav Nayak^{1,*} , Mackenzie Meyer², Gaku Oinuma³, Mark J Kushner^{2,*} 
and Peter J Bruggeman^{1,*} 

¹ Department of Mechanical Engineering, University of Minnesota, 111 Church Street SE, Minneapolis, MN 55455, United States of America

² Electrical Engineering and Computer Science Department, University of Michigan, 1301 Beal Ave, Ann Arbor, MI 48109-2122, United States of America

³ Advanced Technology R & D Center, Mitsubishi Electric Corporation, Hyogo, 661-8661, Japan

E-mail: nayak025@umn.edu, mjkush@umich.edu and pbruggem@umn.edu

Received 27 October 2022, revised 31 January 2023

Accepted for publication 17 March 2023

Published 12 April 2023



Abstract

Charging of particles having diameters of tens of microns has been extensively studied at atmospheric pressure in the context of, for example, electrostatic precipitators where the focus was on unipolar charging. The ambipolar charging of particles in atmospheric pressure plasmas, and of droplets in particular, has received less attention. The plasma activation of droplets is of interest for water purification, fertilizer production and materials synthesis, all of which depend on the transport of the droplets through the plasma, which in turn depends on their charging. In this paper, we report on the transport dynamics of water droplets, tens of microns in diameter, carried by the gas flow through an atmospheric pressure radiofrequency glow discharge sustained in helium. The droplets pass through the plasma with minimal evaporation and without reaching the Rayleigh limit. The droplet trajectory in the presence and absence of the plasma provides insights on the forces acting on the droplet. The measurements were analyzed using results from a three-dimensional fluid model and a two-dimensional plasma hydrodynamics model. We found that the transport dynamics as the droplet enters and leaves the plasma are due to differential charging of the droplet in the plasma gradients of the bounding sheaths to the plasma.

Supplementary material for this article is available [online](#)

Keywords: droplet dynamics, droplet charge, atmospheric pressure plasma

1. Introduction

Dusty plasmas are the focus of fundamental research due to the ability to investigate non-ideal thermodynamic

systems over macroscopic spatial scales and typically consist of micrometer-sized dust grains in addition to the neutral gas, electrons and ions [1–3]. A particle immersed in a low temperature plasma (LTP) acquires a net negative charge to balance electron and positive ion fluxes to its surface, charging the particle to the electrical floating potential. The distribution and fluctuation of dust particles in low pressure plasmas, in which the sheaths surrounding the particle are mostly collisionless, have been extensively investigated using orbital motion limited (OML) theory [4, 5], Monte Carlo simulations [6], stochastic charging models [7], and analytical models

* Authors to whom any correspondence should be addressed.



Original Content from this work may be used under the terms of the [Creative Commons Attribution 4.0 licence](#). Any further distribution of this work must maintain attribution to the author(s) and the title of the work, journal citation and DOI.

[8]. Analytical models have also been developed to estimate the charge on spherical particles in collisional plasmas [9, 10]. Charged microparticles in LTPs have dynamical time scales of tens of milliseconds and can be easily visualized individually [11, 12]. The formation of dust structures or clumps and dust voids (regions devoid of dust particles) in such plasmas have also been investigated, conditions resulting from the balance of the electrostatic and ion drag forces acting on dust particles [11, 13, 14].

Particle dynamics are typically assessed in terms of the forces acting on microparticles immersed in a plasma. These forces are either charge-dependent (ion drag and electrostatic forces) or charge-independent (neutral drag, gravity and thermophoretic forces). In particular, the ion drag force is often of critical importance in low pressure dusty plasmas [15]. The major challenge for determining the electrical forces on a particle is knowing both the charge (Q) on the particle and the electric field (E), both of which may vary with position in the plasma. Beckers *et al* removed this requirement by performing experiments under both normal gravity and microgravity conditions, and assumed that the particle charge scales linearly with the particle radius [16]. Similarly, the charge on microparticles in the afterglow of an inductively coupled low pressure radiofrequency (RF) plasma was determined by applying a known external electric field and measuring the corresponding particle acceleration [17]. Microparticles have also been used as probes to measure the spatially resolved electric field strength and the particle charge in a collisional RF plasma sheath under hypergravity conditions induced by a centrifuge (up to $10g$, $g = 9.81 \text{ m s}^{-2}$) including the use of a collisional sheath model [18].

The plasma activation of water droplets, typically performed at atmospheric pressure, is of interest for water purification [19], fertilizer production [20] and materials synthesis [21, 22], all of which depend on the transport of the droplets through the plasma which in turn depends on their charging. Droplets in atmospheric pressure thermal plasmas have been studied extensively, for example, in the context of surface coatings [23, 24]. However, due to the high gas temperatures ($>2000 \text{ K}$), the plasma-droplet interactions are dominated by thermal effects, and droplet charging in such scenarios is typically not considered to be important [25]. The transport and charging dynamics of micron to tens-of-microns-sized droplets in non-equilibrium LTPs have not been as extensively studied. Given the technological importance of plasma-droplet interactions in non-equilibrium systems, we have performed experimental and computational investigations to provide insights into these transport processes.

Experimental and theoretical studies have been performed to understand the charging and stability of liquid droplets in an applied electric field, mostly related to Coulombic fission and Rayleigh limit/instability [26–31]. Examples include the Taylor experiments demonstrating the fragmentation of water droplets in an applied electric field [26]. Experiments determined the Coulomb fission limit of microdroplets by trapping a droplet in superposed ac and dc electric fields [30] or by

levitating droplets in a double-ring electrodynamic balance [28, 29]. Highly charged droplets are of particular interest due to their use in analytical mass spectroscopy coupled with electrospray ionization [32], and their dynamics have been investigated in this context [32–34]. Most of these studies involve unipolar charging of droplets, which differs from the ambipolar charging that typically occurs in plasmas. In the quasi-steady state ambipolar charging of droplets, the currents of electrons and (positive) ions to the droplet must be balanced. This is accomplished by a transient in which the droplet first charges negatively to the electrical floating potential. Recently, Maguire *et al* investigated the charging of aerosols/droplets in the afterglow of an atmospheric pressure RF plasma jet [35, 36], using an analytical model developed by Khrapak and Morfill [37], applicable for collisional plasmas.

In this paper, we discuss the transport dynamics of liquid water droplets in an atmospheric pressure RF plasma sustained in He, with a focus on the acceleration of the droplets entering and exiting the plasma where the droplets transit through the ambipolar space charge region. Single water droplets are dispensed into the reactor and entrained into the gas flow. In the absence of plasma, the droplets flow with the gas between the parallel plate electrodes at a speed close to the gas velocity. With the plasma operating, we have previously shown that water droplets can be guided through the plasma without significant evaporation and that the droplet charging remains well below the Rayleigh limit to trigger Coulombic fission [19]. These conditions enable us to quantify the forces experienced by the droplet in the plasma. We found that the particle accelerates entering and leaving the plasma as they transit through the ambipolar space charge regions at the top and bottom of the plasma. Using charge on the droplet provided by analytic theories and modeling, these accelerations require electric fields of $(1 - 2) \times 10^5 \text{ V m}^{-1}$. We propose that the source of these electric fields is the differential charging of the droplet in the plasma gradients at the top and bottom of the plasma. This differential charging produces asymmetric electric fields in the sheaths at the top and bottom of the droplet, which produces a net force that accelerates the droplet.

The experiment and models used in this investigation are described in section 2. The transport dynamics of droplets in the RF plasma are discussed in section 3. Our concluding remarks are in section 4.

2. Descriptions of the experiment and models

2.1. Plasma reactor

A detailed description of the plasma reactor used in this investigation can be found in [19, 38, 39]. In brief, an RF-driven (13.56 MHz) capacitively-coupled diffuse glow discharge is generated between two parallel water-cooled copper electrodes embedded inside a polytetrafluoroethylene housing (see figure 1). The cross-sectional area of the electrodes is $19.1 \times 9.5 \text{ mm}^2$ with an inter-electrode spacing of 2 mm. The

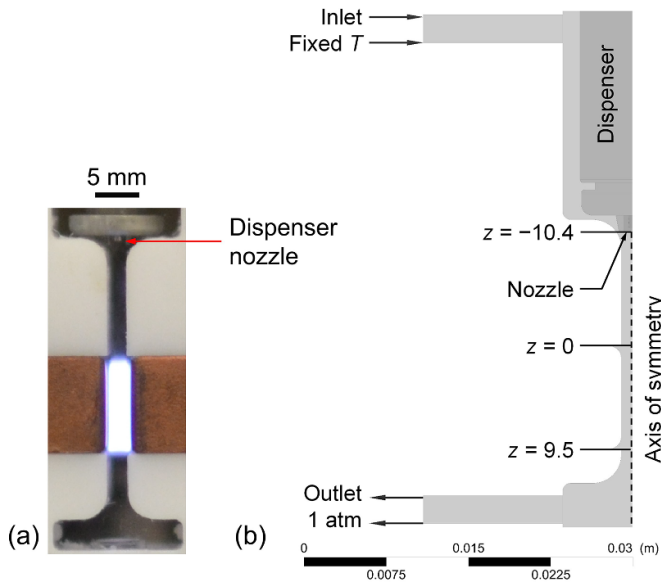


Figure 1. Plasma reactor. (a) Image of the RF plasma reactor in operation including the copper electrodes and the droplet dispenser. (b) Cross section of the 3D model geometry used for the fluid simulation. The fluid domain is shown in light grey color, while the dark grey region represents the droplet dispenser domain (not modeled). The top and bottom edges of the electrode are shown at $z = 0$ and $z = 9.5$ mm.

plasma was generated within this gap in different gas admixtures of helium (ultra-pure carrier grade 99.9995%) at atmospheric pressure with total gas flow rates ranging from 0.5 to 3.0 standard liters per minute (slm) using mass flow controllers (MKS, GE50A). The plasma power was measured from the voltage and current waveforms recorded on a digital oscilloscope (Tektronix DPO2024B, 200 MHz, 1 GS^{-1}) using a high bandwidth voltage probe (Tektronix P5100A, 500 MHz, $100\times$, 2.5 kV) and a current transformer (Pearson Electronics, Model 2878) located at the powered RF connection between the matching box and the reactor.

2.2. Droplet generation and imaging

Single deionized water droplets, tens of microns in size, were generated by an on-demand dispenser (MicroFab Technologies Inc. MJ-ATP-01-070) enclosed in an aluminum casing and mounted on top of the plasma reactor as shown in figure 1(a). The droplet ejection frequency, diameter and initial velocity were governed by the piezoelectric actuation, which was triggered by tailored trapezoidal waveforms generated by an external controller (MicroFab Technologies Inc. JetDrive™ III CT-M5-01). The droplet ejection frequency was fixed at 100 Hz in this study. The droplets were then carried downward with the gas flow between the electrodes.

The inter-electrode gap through which the droplets traversed was optically accessible for imaging of the droplets through quartz windows enclosing the electrode surfaces. The trajectory or dynamics of the micro-droplets through the

reactor were monitored by microscopic imaging using a fast-framing camera (Photron FASTCAM Mini UX50) located at the front of the reactor, while an LED flashlight located behind the reactor illuminated the path of the droplets. The camera was mounted with a micro-focus lens (Nikon Micro-Nikkor 105 mm) and an extension tube of length 200 mm to obtain a high magnification and an image resolution of $1.7 \mu\text{m}/\text{pixel}$. The camera settings (16 000 frames per second and shutter speed of $7.8 \mu\text{s}$) were fixed throughout this work. The recorded video data were analyzed by the image analysis software, NIH ImageJ [40], the details of which are outlined in [19]. The variations in the droplet trajectory were assessed at different locations along the droplet trajectory by moving the reactor vertically using a micrometer-controlled linear translational stage. Time-resolved data were extracted from the position and local velocity of the droplets.

2.3. Modeling of gas dynamics

A three-dimensional computational fluid dynamics (CFD) model of the reactor was developed using the commercial software ANSYS-CFX, to simulate the gas velocity within the reactor channel. The geometry of the fluid domain is symmetric across two planes normal to each other at the center of the reactor. As a result, only a quarter of the entire geometry was used for the simulation. The geometry used in the model corresponding to the experiment is shown in figure 1(b) including the boundary conditions. A constant mass flow rate corresponding to the volumetric flow of 1 slm and a fixed gas temperature of 295 K was used for the inlet conditions, while an opening to the ambient at a static pressure of 1 atm was used as the outlet condition. For a gas flow rate of 1 slm, the Reynolds number (Re) is ~ 21 , and so a laminar flow model was used.

2.4. Measurement of electron properties

The electron density (n_e) and temperature (T_e) in the He plasma were determined from the emissivity measurements of the continuum (neutral bremsstrahlung) radiation without the droplets in the plasma [38, 41, 42]. The time and spatially averaged absolute total plasma emission was recorded by optical emission spectroscopy using a calibrated tungsten halogen lamp, the details of which can be found in [38]. The shape and magnitude of the absolute plasma emission (continuum) intensity were fitted with the electron-atom bremsstrahlung radiation with a non-Maxwellian distribution of electron energies to determine n_e and T_e . An example of this fitting of the emissivity with the experimentally measured absolute intensity of the continuum radiation is shown in figure 2. The conditions are a He plasma operated at 1 slm and 14 W without droplets. An electron density of $1.2 \times 10^{17} \text{ m}^{-3}$ was obtained for an electron temperature of 3.5 eV. The uncertainty in T_e is ± 1.3 eV, a value that is fairly large due to the presence of atomic and molecular emission lines and bands. The corresponding n_e will vary in the range of $(0.8 - 2.8) \times 10^{17} \text{ m}^{-3}$.

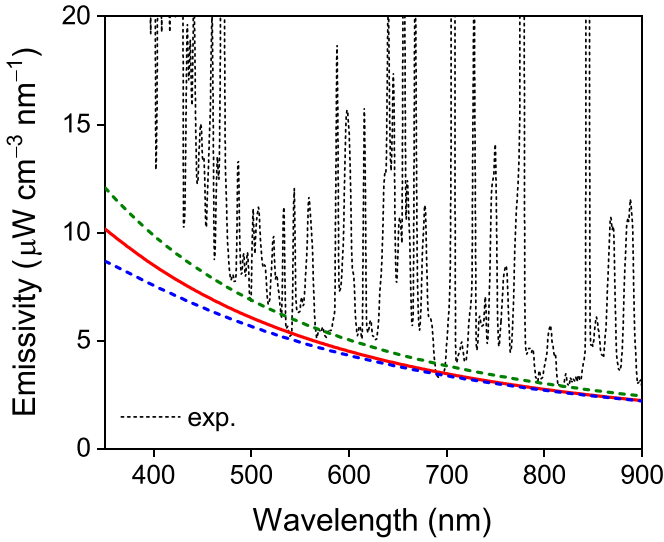


Figure 2. Electron properties (n_e , T_e) were derived from continuum radiation measurements in a He plasma at a discharge power of 14 W and gas flow rate of 1 slm. The red line fit corresponds to $T_e = 3.5$ eV and $n_e = 1.2 \times 10^{17} \text{ m}^{-3}$, while the blue and the green dashed lines represent the uncertainty of the emissivity fitting.

Using this method for determining T_e gives the temperature of the electrons at the location of the radiating states, which are primarily located at the sheath edges and not in the bulk plasma, and overestimates the bulk T_e .

2.5. 2-dimensional plasma model

The plasma reactor with an embedded droplet was simulated using *nonPDPSIM*, a 2-dimensional (2D) plasma hydrodynamics model. Using an unstructured mesh, *nonPDPSIM* solves for electric potential, charged species densities, T_e , and neutral species densities. Using the stationary solution of Boltzmann's equation, for a range of E/N (electric field/gas number density), rate coefficients for electron-impact processes are calculated and used to generate a lookup table as a function of T_e . The power deposition in the plasma was calculated as the volume integral of $\vec{j} \cdot \vec{E}$ (current density times electric field). The applied voltage was adjusted after each RF (13.56 MHz) cycle to produce 15 W of power deposition. Results are reported after over 200 RF cycles. A more detailed description of *nonPDPSIM* can be found in Norberg *et al* [43].

The reactor geometry used in the model is shown in figure 3(a). The mesh has a total of 11236 nodes and 7328 nodes in the plasma region. A single 40 μm diameter droplet was placed near the bottom edge of the electrodes, centered within the plasma gap. The droplet was modeled as a non-conductive dielectric with relative permittivity of 80 (matching that of water). Saturated vapor pressure of H_2O was maintained at the surface of the droplet as well as the collector plate at the bottom of the reactor. In this 2D Cartesian geometry, the droplet appears as a cylinder.

The plasma is sustained in He with 7.5 ppm O_2 and 2.3 ppm H_2O . While experimentally reported impurities were 1.5 ppm O_2 , 6 ppm N_2 , and 2.3 ppm H_2O [39], the N_2 impurity was

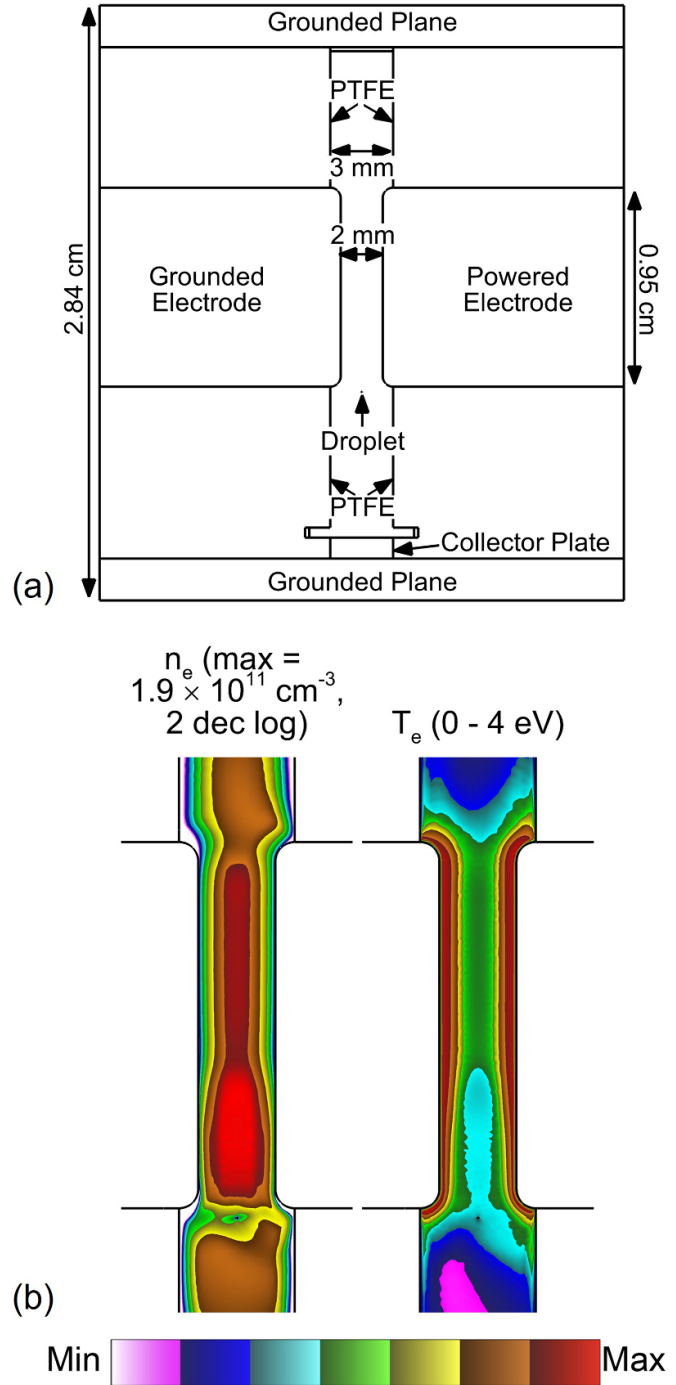


Figure 3. (a) Geometry, and (b) plasma properties (n_e and T_e averaged over one RF cycle) for the base case produced by *nonPDPSIM*.

removed in the calculation to decrease computational complexity. The reaction mechanism contains 47 species, with 20 charged species, and 805 reactions. The reaction mechanism is based on Van Gaens and Bogaerts [44] with updates from Norberg, Emmert *et al*, and Lietz *et al* for He [45–47]. The species used in the model are listed in table 1. Evaporation of H_2O from the surface of the droplet was computed for the residence time of the droplet before the plasma calculation began, resulting in a ring of H_2O around the droplet. The H_2O density

Table 1. Species included in the 2D plasma simulations.

Charged species	$e, H^+, H_2^+, OH^+, OH^-, H_2O^+, H_3O^+, O_2^+, O_2^-, O^+, O^-, H_2O^+(H_2O), O_2^+(H_2O), H_3O^+(H_2O), O_2^-(H_2O), O^-(H_2O), OH^-(H_2O), He^+, He_2^+, HeH^+$
Neutral species	$H, H_2, OH, H_2O, HO_2, H_2O_2, O_2, O, He$
Excited states	$H^*, H_2(r), H_2(v), H_2^*, OH(A^2\Sigma), H_2O(v), O_2(v), O_2(r), O_2(^1\Delta), O_2(^1\Sigma), O(^1D), He(2^3S), He(2^1S), He(2^3P), He(2^1P), He(3P), He(3S), He_2^*$

decreases with distance from the droplet. In the simulations, the droplet is static and does not traverse the reactor. That said, the evaporating water from the droplet will translate with the droplet in the bulk gas flow. As a result, evaporation from the static droplet is a good representation of the flowing system.

The electron density and T_e with the droplet present are averaged over one RF cycle as shown in figure 3(b). The droplet was placed at the bottom edge of the electrodes. The electron density is maximum between the electrodes and increases in the bottom half of the electrode gap. Due to the ring of evaporating H_2O surrounding the droplet, there is additional H_2O in the bottom of the electrode gap relative to the top. The increased H_2O density increases the electron density as H_2O has a lower ionization threshold than He and undergoes Penning ionization with excited states of He. T_e is the highest in the sheaths near the electrodes and varies significantly over the RF cycle, reaching an instantaneous maximum of 5.8 eV. The emissivity predicted by the results of *nonPDPSIM* matches the experimental measurements in this system [48].

3. Transport dynamics of droplets transiting the plasma

3.1. Droplet dynamics

The droplet dynamics were captured and analyzed as described in section 2.2. Figure 4 shows the motion of a droplet in a He plasma recorded at the bottom part of the electrode with an initial diameter of $42 \mu m$ traversing in gas flow rates ranging from 0.50 to 3.0 slm. In the case of 0.50 slm, the droplet experiences deceleration at the bottom of the electrode to the point that it is deflected and starts to move in the direction opposite to the gas flow. The negatively charged droplets are trapped in the plasma by electrical forces at the edge of the plasma, such as the ambipolar field (see further), producing an acceleration upwards and the gas flow and gravity, producing a force downwards. A minimum gas flow rate of 0.75 slm is required to provide a large enough downward force for the droplet to exit the plasma as shown in figure 4(b).

The corresponding droplet velocities in the axial direction derived from images as shown in figure 4 are shown in figure 5. Recall that the nozzle of the dispenser is at -10.4 mm and the bottom of the reactor is at 15 mm. The top of the electrode is at 0 mm and the bottom of the electrode is at 9.5 mm. A positive velocity here refers to the droplet moving downwards through the reactor. Reference velocities are also shown when

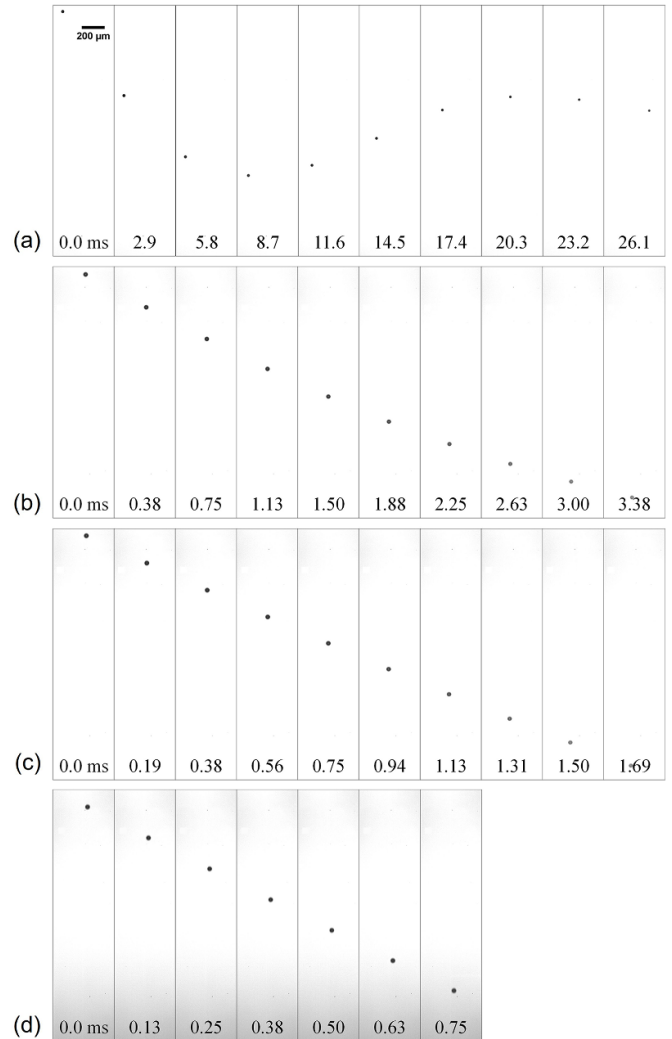


Figure 4. Time variation of the motion of a droplet ejected at 100 Hz with an initial diameter of $42 \mu m$ and a velocity of $\sim 0.5 \text{ m s}^{-1}$ in a He plasma operating at 14 W with gas flow rates of (a) 0.50, (b) 0.75, (c) 1.5 slm, and (d) 3.0 slm. The timestamp shown at the bottom of each image is in units ms. The center of each frame is located at $z = 9.5$ mm (see figure 1). The images for the 0.50 slm case in (a) span a longer time interval than the images of the other gas flow rates.

the plasma is off. While with a flow rate of 0.75 slm, the droplet is decelerated at the bottom edge of the electrode, its velocity still remains positive through its trajectory. The droplet is accelerated by electric fields at the periphery of the plasma into the bulk plasma for all gas flow rates although with more

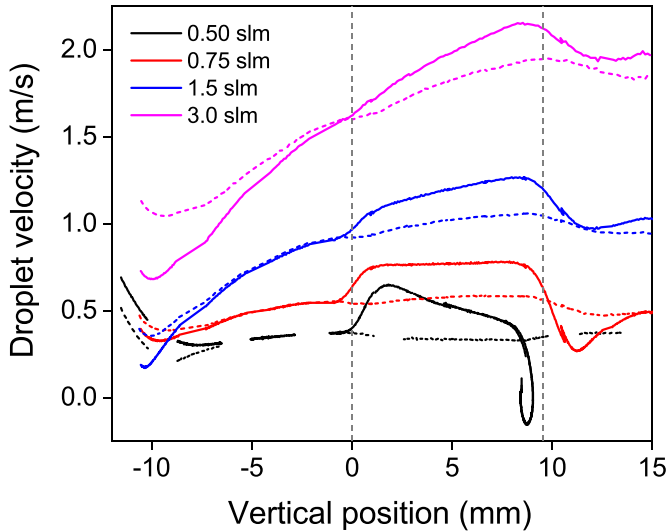


Figure 5. Droplet velocity as a function of droplet position in a He plasma operating at 14 W with gas flow rates of 0.50, 0.75, 1.5 and 3.0 slm. The top of the reactor is at -12.5 mm. The bottom of the reactor is at 15 mm. The ‘gas only’ condition is shown by dotted lines, while the solid lines represent the ‘plasma on’ condition. The dashed grey vertical lines represent the top and bottom edges of the electrodes.

pronounced accelerations for the lowest gas flow rates. This acceleration is consistent with droplets acquiring a negative charge as they approach the plasma in the space charge region at the edge of the plasma. The rate at which the droplet decelerates while exiting the plasma ($z = 9.5$ mm) decreases with increasing gas flow. These trends suggest that the drag force on the droplet starts to dominate the electrical force at higher gas flow rates. In comparison, when the plasma is off, these regions of acceleration and deceleration are absent, consistent with the droplet being carried by the gas flow.

The forces acting on the droplet during its flight through the plasma are shown in figure 6. In the absence of the plasma, the force balance on the droplet is

$$m_p \frac{dv_p}{dt} = F_g - F_d + F_0 \delta(t - t_0) \\ = (\rho_p - \rho_{\text{gas}}) \frac{\pi d_p^3}{6} g - \frac{3\pi\eta d_p}{C_c} (v_p - v_{\text{gas}}) + F_0 \delta(t - t_0), \quad (1)$$

where F_g , F_d , and $F_0 \delta(t - t_0)$ are the gravitational force due to the mass (m_p) of the droplet, the neutral drag force due to entrainment in the flowing gas, and an initial droplet ejection acceleration term, respectively. The initial time of ejection, $t_0 = -20.4$ ms, is the time at which the droplet is produced from the nozzle. This initial acceleration term was determined at $t = t_0$ by substituting the term v_{gas} in equation (1) with the value obtained from the gas flow CFD simulation at the tip of the nozzle and had a value of 0.74 nN. Other terms in the expression are known from measurements: ρ_p , ρ_{gas} , d_p , g , v_p , v_{gas} and η are the droplet density, gas density, droplet diameter,

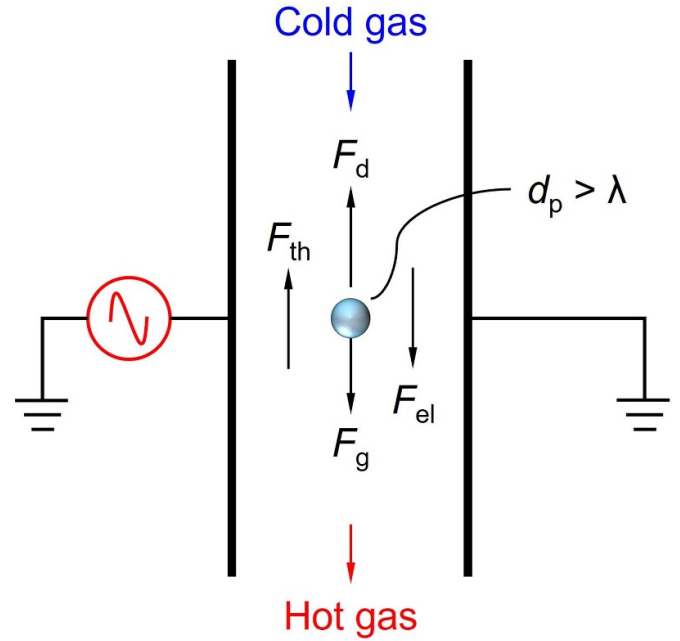


Figure 6. Schematic of forces acting on a droplet in the plasma: F_d (fluid drag), F_g (gravity), F_{el} (electrical), F_{th} (thermophoretic). The gas flows through the electrode gap from top to bottom while being heated by the plasma, hence, cold gas entering the plasma and hot gas leaving the plasma.

the gravitational constant, droplet velocity, gas velocity, and kinematic viscosity of the surrounding gas, respectively. C_c is the slip correction factor and is equal to $1 + 2.52\lambda/d_p$, with λ the mean free path of the gas [49]. The neutral drag force depends on the relative velocity of the droplet. Since for a droplet of diameter $42 \mu\text{m}$, the particle Reynolds number (Re) is 0.016 (< 1.0) with a terminal settling velocity of 0.046 m s^{-1} , the droplet motion is within the range of Stoke’s law used to describe F_d . The movement of ions in the plasma can also impart a force to the droplet, more commonly known as the ion drag. However, due to the high collisionality at atmospheric pressure, the low ion drift speeds, and the small mean free path, less than $1 \mu\text{m}$, ion drag forces are not important. These forces are dominantly perpendicular to the electrodes and so perpendicular to the droplet movement.

3.2. Initial droplet acceleration

The droplet velocity in the presence and absence of the plasma is influenced by the velocity at which the droplet is initially injected ($v_{p,i}$) into the gas from the dispenser or its initial acceleration. The gas flow field produced by the CFD calculations is shown in figure 7. The effect of $v_{p,i}$ on the spatial droplet velocity in a He + 0.2% H₂O gas mixture at different gas flow rates is shown in figure 8(a) without the plasma (‘gas only’) and (b) with the plasma. The higher $v_{p,i}$ in ‘gas only’ and plasma cases is $\sim 1.7 \text{ m s}^{-1}$ and $\sim 1.2 \text{ m s}^{-1}$, respectively, while the lower $v_{p,i}$ is $\sim 0.4 \text{ m s}^{-1}$ in both cases. From figures 7 and 8(a), for $v_{p,i} \approx 1.7 \text{ m s}^{-1}$, $v_p \gg v_{\text{gas}}$. The resulting F_d decelerates the

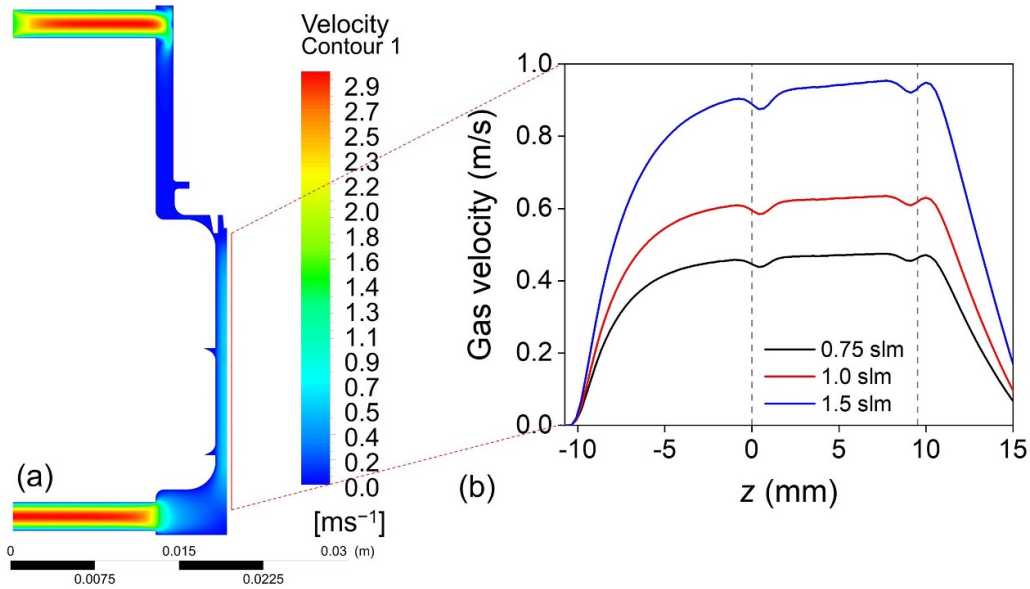


Figure 7. Flow field properties obtained from CFD simulations. (a) Gas velocity contours for He at 1 slm and 295 K, and (b) corresponding gas velocity at 0.75, 1.0 and 1.5 slm as a function of height on the central axis of the reactor. The dashed vertical grey lines represent the top and bottom edges of the electrodes.

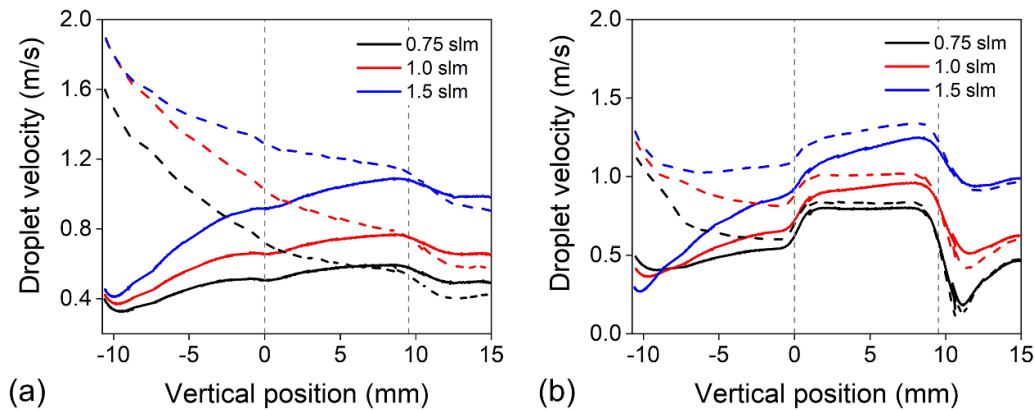


Figure 8. Spatial variation in the measured droplet velocity ($d_p = 42 \mu\text{m}$) for low (solid line) and high (dashed line) initial ejection velocities of the droplet from the dispenser ($v_{p,i}$) at different gas flow rates in He + 0.2% H₂O (a) without plasma ('gas only'), and (b) with plasma (14.3 W). The dashed grey lines indicate the top and bottom edges of the electrode.

droplet to bring the droplet velocity to the same magnitude as the gas velocity. However, for $v_{p,i} \approx 0.4 \text{ m s}^{-1}$, $v_p < v_{\text{gas}}$, and F_d accelerates the droplet to the gas velocity. Even with a significant reduction in the droplet velocity with higher $v_{p,i}$ at $z < 0 \text{ mm}$, v_p both with and without the plasma ($0 < z < 9.5 \text{ mm}$) is higher than the v_p produced with lower $v_{p,i}$. This is because inertia is important on the timescales of the droplet moving through the reactor. The droplet velocity relaxation time (τ) is given by [49]:

$$\tau = \frac{\rho_p d_p^2 C_c}{18\eta}. \quad (2)$$

The relaxation time for a droplet of diameter $42 \mu\text{m}$ is 5 ms for the experimental conditions, similar to the droplet residence time in the reactor ($t_{\text{res}} = 10.9 \text{ ms}$), indicating that the droplet inertia plays an important role in the droplet dynamics. Due to the importance and influence of the initial droplet

acceleration, we focus on a low injection velocity case to quantitatively explain the droplet behavior and the forces experienced by the droplet.

3.3. Droplet and gas velocity without plasma

To quantitatively explain the droplet behavior, it is necessary to first quantify the gas velocity flow field. The helium gas flow field was simulated as described in section 2.3. The resulting flow field gas velocity for a He flow rate of 1.0 slm is shown in figure 7(a). The inlet and outlet have smaller flow cross section than the outer regions of the reactor and hence a significantly larger gas velocity is observed. The corresponding v_{gas} along the axis of symmetry for gas flow rates of 0.75, 1.0, and 1.5 slm is shown in figure 7(b). For low gas flow rates (0.75 and 1.0 slm), the gas accelerates until the top edge of the electrode ($z = 0 \text{ mm}$), and reaches a steady state thereafter. For

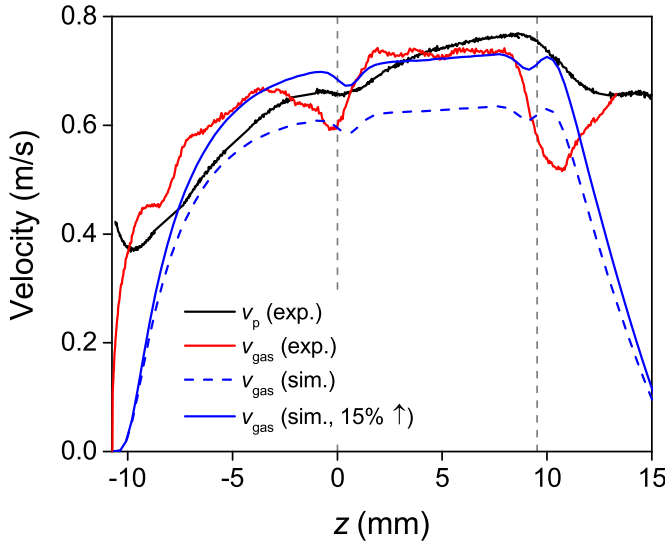


Figure 9. Simulated and measured gas velocities with He gas at 1 slm and 295 K without plasma, and measured velocity of a droplet (v_p) with a diameter of $42 \mu\text{m}$ as a function of the droplet position along its trajectory, z . The dashed vertical grey lines represent the top and bottom edges of the electrodes.

the higher gas flow rate of 1.5 slm, the gas has an appreciable acceleration even in the electrode region ($0 < z < 9.5 \text{ mm}$) suggesting that the gas flow under these conditions is not fully developed.

The measured droplet velocity (v_p) in He gas at 1.0 slm without the plasma is shown in figure 9. In addition to the simulated gas velocity (obtained by CFD), we can determine the gas velocity experimentally by balancing the forces acting on the droplet in the absence of plasma using equation (1). The computationally and experimentally obtained gas velocities are also shown in figure 9. The measured gas velocity reaches two maxima, one before and one after entering the electrode region. The second maximum corresponds to a steady-state gas velocity of a fully developed flow in the channel. With exception of an initial deceleration, the droplet velocity follows the gas velocity. However, v_p is larger than v_{gas} by $\sim 0.04 \text{ m s}^{-1}$ in the electrode region, consistent with the calculated $v_p - v_{\text{gas}} \approx 0.05 \text{ m s}^{-1}$ in the absence of droplet acceleration from equation (1). The gravitational force results in the droplet velocity being larger than the gas velocity. At $z > 9.5 \text{ mm}$, v_p reduces to be similar to v_{gas} due to the widening of the channel, but at a slower rate due to the inertia of the droplet.

When comparing the calculated gas velocity with the experimentally derived gas velocity, large discrepancies are found (figure 9). Due to a combined uncertainty of $\sim 15\%$ in the mass flow controller ($\pm 1\%$ accuracy of full scale leading to a total inaccuracy of $\pm 3\%$ with a 3000 sccm MFC, $\pm 0.3\%$ repeatability, 0.1% resolution error, and uncertainty in the calibration factor of He as opposed to N_2 used for calibrating the MFC), the uncertainty in the geometry of the inter-electrode spacing ($\sim 200 \mu\text{m}$ mounting to $\sim 10\%$ of the geometrical uncertainty), and the intrinsic accuracy of the CFD simulation itself used in this work, the gas flow was also simulated at a 15% larger gas flow rate (1.15 slm), which reproduces the experimental

v_{gas} when in steady-state. For further analysis, the simulated v_{gas} obtained from the 15% increase in the mass flow rate will be used. Nonetheless, major differences in the transients near the electrode edges remain although rapid variations cannot be accurately measured with the used approach due to droplet inertia.

The rounded electrode edges were included in the model to represent the actual electrode geometry as used in the experiments. The rounded edges produced local changes in the gas velocity. While an inconvenience in this experiment, the rounding of the edges was necessary to prevent a glow-to-spark transition. The simulated v_{gas} was also able to capture the deceleration experienced by the droplet at $z = 0 \text{ mm}$ to some extent.

3.4. Droplet and gas velocity with plasma

Plasma-induced gas heating will impact the gas flow velocity. The spatial gas temperature distribution has been measured previously in He/ H_2O plasma [19] and He/Ar/ H_2O plasma [50], while the steady-state gas temperature was measured in He and He/Ar plasmas [38, 39]. The gas velocity in the presence of the plasma will be determined from the force balances and fluid model as detailed below.

To account for gas heating, we need to correct the gas velocity in the presence of the plasma. Considering mass continuity, the mass flow rate ($\dot{\varphi}$) at any axial position within the flow field is given as

$$\dot{\varphi} = \int \rho(x, y, z)v(x, y, z)dA = \text{constant}. \quad (3)$$

Assuming the velocity profile is not altered, and gas heating is radially homogeneous, the gas velocity in the presence of plasma is given as

$$v_{\text{gas}}(z) = \frac{\rho(0)}{\rho(z)}v_{\text{gas}}(0) = \frac{T_{\text{gas}}(z)}{295}v_{\text{gas}}(0). \quad (4)$$

Measured and simulated v_{gas} from the ‘gas only’ case (figure 9) were used in equation (4), along with a measured gas temperature profile in the electrode region of a pure He glow plasma having a steady-state value of $\sim 340 \text{ K}$ [39]. The scaled-up gas velocities were determined and are shown in figure 10. Assuming that the steady-state is reached within the electrode region, the difference between the droplet and the gas velocities would still hold in the presence of plasma ($v_p - v_{\text{gas}} \approx 0.05 \text{ m s}^{-1}$). The gas velocities (experimental and simulated) can be corrected to reach the same steady-state value (inertia term becomes zero) by imposing a gas temperature profile with a higher steady-state value of 365 K instead of 340 K. These ‘corrected’ velocities and gas temperature are also shown in figure 10. The correction of 25 K is within the typical uncertainty of gas temperature measured by optical measurements of the ro-vibrational spectra of OH(A) molecular band [51]. However, a higher axial velocity than obtained by equation (4) is expected due to the non-homogeneous velocity and gas temperature profile.

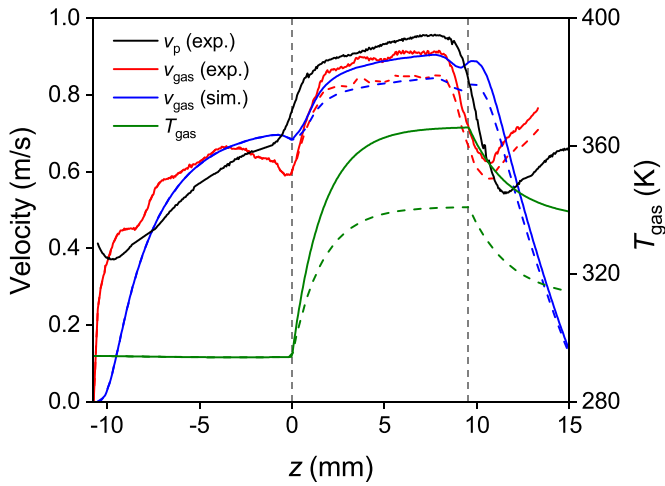


Figure 10. Measured and simulated gas velocities as a function of the droplet position for a gas flow rate of 1 slm in He at 14 W. Both the original ($T_{\max} = 340$ K, dashed line) and corrected ($T_{\max} = 365$ K, solid line) gas velocities are shown. The correction was made to enable consistency with the measured steady-state droplet velocity. The dashed vertical grey lines represent the top and bottom edges of the electrodes.

In the presence of a plasma, in addition to F_g and F_d , the droplet also experiences an electrical force (F_{el}) due to the ambipolar electric field at the edges of the plasma. With an axial gas temperature gradient, the droplet experiences a thermophoretic force (F_{th}) directed from hotter to cooler gas [52]. For a droplet with $d_p > \lambda$, the droplet dynamics in the presence of plasma are given by

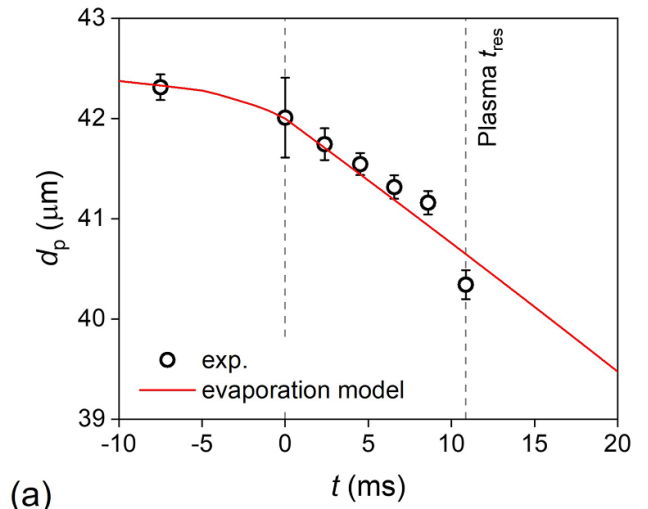
$$\begin{aligned} m_p \frac{dv_p}{dt} &= F_g - F_d - F_{th} + F_{el} + F_0 \delta(t - t_0) \\ &= (\rho_p - \rho_{gas}) \frac{\pi d_p^3}{6} g - \frac{3\pi\eta d_p}{C_c} (v_p - v_{gas}) \\ &\quad - \frac{9\pi d_p \eta^2 H \nabla T}{2\rho_{gas} T} + QE(z) + F_0 \delta(t - t_0) \end{aligned} \quad (5)$$

where Q , $E(z)$, T , and ∇T [K m^{-1}] are the charge on the droplet, the time-averaged electric field, the gas temperature, and the temperature gradient in the plasma, respectively. H is an accommodation term that includes the effect of the temperature gradient inside the droplet given by [49, 52] as

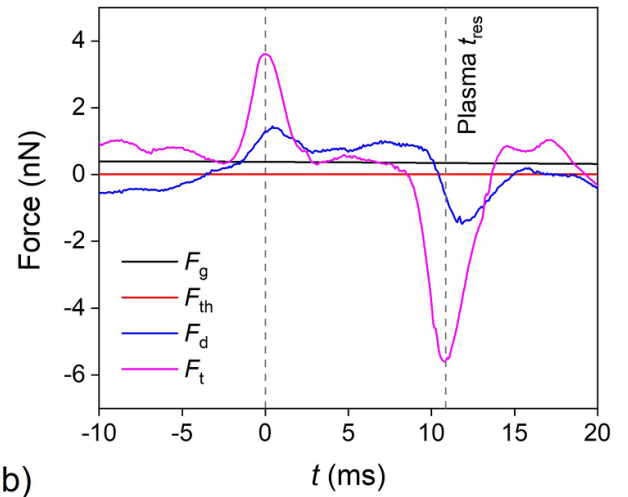
$$H = \left(\frac{1}{1 + 6\lambda/d_p} \right) \left(\frac{k_{gas}/k_p + 4.4\lambda/d_p}{1 + 2k_{gas}/k_p + 8.8\lambda/d_p} \right), \quad (6)$$

where k_p and k_{gas} are the thermal conductivity of the droplet and the gas, respectively.

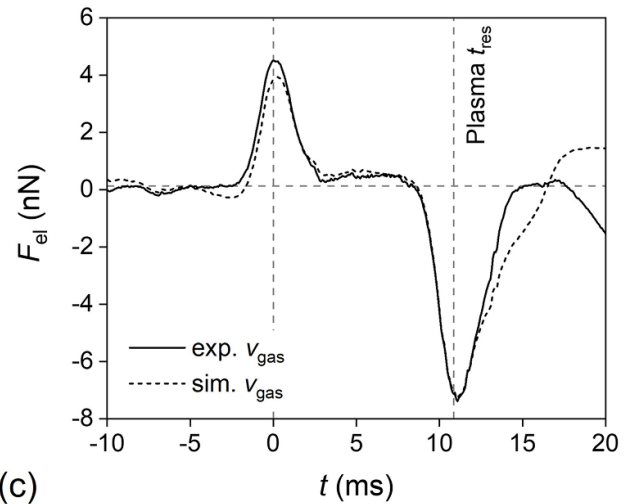
To evaluate F_g , F_d and F_{th} in equation (5), the droplet diameter, which changes more significantly in the presence of a plasma, as a function of time is obtained by fitting the measured droplet diameters at different locations (figure 1(a)) [50] using a droplet evaporation model discussed in [19] and [49]. The time evolution of the droplet diameter in a He plasma at 1 slm and 14 W is shown in figure 11(a). With the known v_p ,



(a)



(b)



(c)

Figure 11. Droplet properties and forces. (a) Time evolution of droplet diameter, (b) forces acting on the droplet in the He plasma operating at 14 W and flow rate of 1 slm, and (c) the electrical force (F_{el}) on the droplet derived from equation (5) using the corrected v_{gas} from figure 10. F_{el} from the experimentally obtained v_{gas} and simulated v_{gas} are shown in solid and dashed lines, respectively. The dashed vertical grey lines indicate the times when the droplet passes the top and bottom edges of the electrodes.

v_{gas} , T_{gas} , ∇T and other associated parameters, the individual forces on the droplet can be determined. The time evolution of these forces is shown in figure 11(b). The thermophoretic force is the weakest with a magnitude of a few pN and can be neglected for the conditions. The gravitational force is a few tenths of a nN and the neutral drag force is of the order of a nN. The total force on the right-hand side of equation (5) causing droplet acceleration (F_t) is obtained from the first derivative of v_p , which is of the order of a few nN at $t = 0$ and $t = 10.9$ ms, corresponding to times at which the droplet enters and exits the plasma.

Using these values for the forces in equation (5) at a steady-state T_{gas} of 340 K, F_{el} can be determined, and is shown in figure 11(c) for both the experimentally derived and simulated v_{gas} . In spite of significant differences in the measured and simulated v_{gas} at $t = 0$ and $t = 10.9$ ms, F_{el} in both cases are similar suggesting that the discrepancies are due to slow varying effects. There is no electrical force on the droplet before entering the plasma, while the axial electric field is expected to be very small in the bulk plasma. However, F_{el} is non-zero (0.45 ± 0.07 nN) in the bulk of the plasma region as shown by the dashed lines in figure 11(c). This non-zero F_{el} is attributed to the uncertainty in the correction of the gas velocity due to gas heating, which in turn significantly impacts the derived F_{el} in the bulk plasma. As F_{el} determined from experimentally derived and simulated v_{gas} are similar, we will use the experimentally derived v_{gas} in further discussions.

3.5. Estimate of the droplet charge

In order to estimate the axial electric field ($E(z)$) from F_{el} , the droplet charge (Q) is required. This value can be estimated using the relation $Q = C\phi_p$, where ϕ_p is the potential at the surface of the droplet relative to the bulk plasma, and C is the capacitance of the droplet, which is equal to that of a spherical capacitor, $C = 2\pi\epsilon_0 d_p$. With a typical electron current to the droplet of $10^{12} - 10^{13} \text{ s}^{-1}$ and a corresponding estimated charge on the droplet of $\sim 10^5 e$ (see discussion below), it takes $\sim 10 - 100$ ns to charge a droplet of diameter $42 \mu\text{m}$. This characteristic charging time is much shorter than the timescale of the droplet dynamics, and so we assume the charge on the droplet is equal to the steady-state charge in the bulk of the plasma.

The charge density on the droplet located near the bottom edge of the electrode from *nonPDPSIM* is shown in figure 12(a). This charge density is time-averaged over one RF cycle. The high dielectric constant of the water droplet leads to polarization in the applied electric field in the horizontal direction. With drift speeds of electrons being dominant in the horizontal direction, the end results are non-uniform surface charge densities. The charge on the cylindrical ‘droplet’ is $-4.0 \times 10^7 e \text{ cm}^{-1}$. The total charge is then $-7.7 \times 10^7 e$, obtained by multiplying by the depth of the reactor in the simulation (1.91 cm). To convert this charge to the equivalent charge on a spherical droplet, we scale by the ratio of the surface area of the spherical droplet to the surface area of the

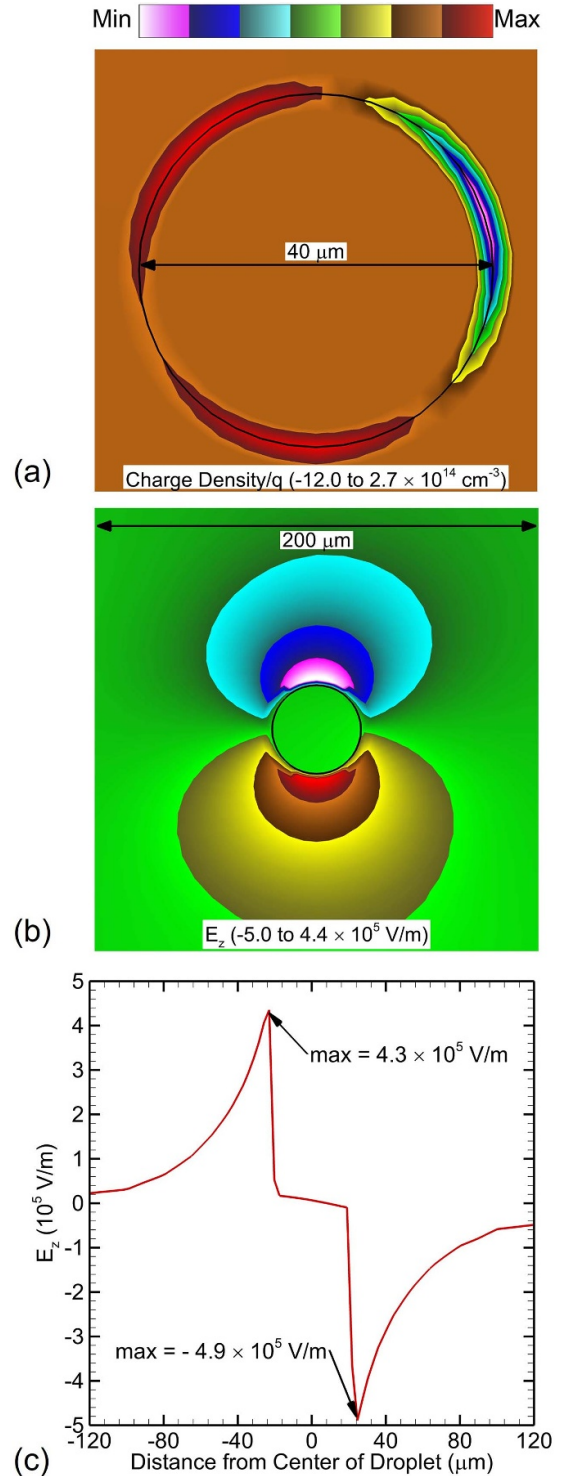


Figure 12. Simulated time-averaged plasma properties in the vicinity of a $40 \mu\text{m}$ diameter droplet. (a) Charge density on the droplet, (b) axial electric field, and (c) axial electric field along a vertical line through the center of the droplet.

cylinder. The charge on a $40 \mu\text{m}$ diameter spherical droplet predicted by the model would then be $-1.1 \times 10^5 e$.

As shown in our previous work, a droplet immersed in the center of an RF glow discharge will asymmetrically charge

Table 2. Parameters used to estimate the electric field using plasma parameters obtained from continuum radiation and the analytical model as well as 2D *nonPDPSIM*.

Parameters	Continuum radiation and analytical model	<i>nonPDPSIM</i>
Q (e)	$-(2.6 \pm 0.9) \times 10^5$	-1.1×10^5
n_e (m^{-3})	$1.2 \frac{+1.6}{-0.4} \times 10^{17}$	1.2×10^{17}
T_e (eV)	3.5 ± 1.3	1.8
n_- (m^{-3})	–	3.5×10^{15}
n_+ (m^{-3})	$1.2 \frac{+1.6}{-0.4} \times 10^{17}$	1.3×10^{17}

(negative at the equator and positive at the poles) [48]. The asymmetric charging results from the differing contributions to charged particle transport to the surface of the droplet at the equator and poles. Along the equator of the droplet, the electron motion is dominated by drift in the electric field. The horizontal electric field is enhanced along the equator and decreased at the poles by polarization of the droplet. The sheath electric field points towards the droplet whereas the horizontal electric field alternates direction during the RF cycle. As a result, during the RF cycle, the horizontally applied electric field and the sheath electric field are aligned or opposed, either intensifying the total electric field or, in some cases, reducing the field to zero. At the poles, the electron motion towards the surface of the droplet is dominated by diffusion. While the droplet here is positioned at the lower edge of the plasma instead of being immersed in the center of the plasma, the asymmetric charging is still seen.

The droplet potential and the charge on the surface of the droplet immersed in the plasma can also be estimated from the electron and ion fluxes to the surface of the droplet by analytical models [36, 37, 53–55]. These models require knowledge of the electron temperature and density in the bulk plasma which was taken from the continuum emission measurements (see table 2). While such models use many different assumptions, a comparison of 5 different models reported in literature shows that the variation of the deduced droplet charge remains below 25%, with the exception of the collisionless OML theory (see sheath model 1 in the Supporting Information) due to the assumption that the ions are collisionless. Even more, while the analytical models assume steady-state conditions, they do not consider RF variations or asymmetric charging as found in *nonPDPSIM*. As such the obtained droplet charge overestimates the *nonPDPSIM* result but remains within a factor of 3.

The plasma properties from *nonPDPSIM* are also shown in table 2. For all properties except the charge on the droplet, Q , the values from *nonPDPSIM* are extracted from the center of the electrode gap at the midpoint of the electrodes. The electron density from the experiment is in excellent agreement with the model but the experimentally derived electron temperature is an overestimation (due to spatial averaging and including emission of the near sheath regions). If we use the

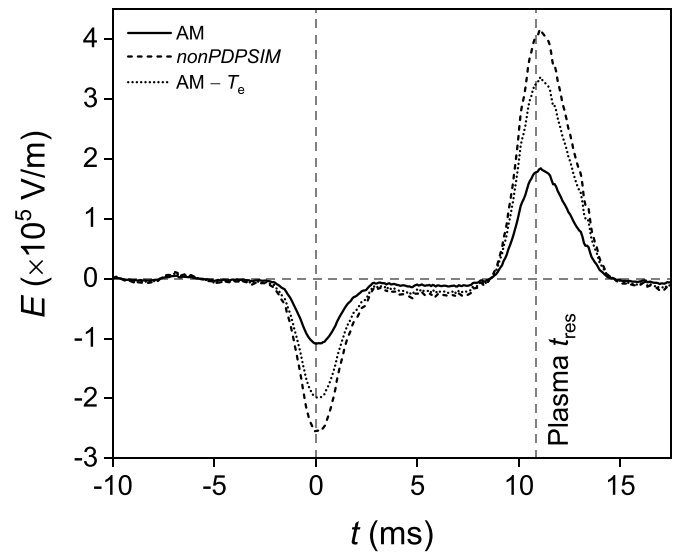


Figure 13. Electric fields obtained in He plasma operating at 1 slm and 14 W, for measured T_e of 3.5 eV and n_e of $1.2 \times 10^{17} m^{-3}$ from the continuum measurements using the droplet charges obtained from the analytical ion continuum model [54] (AM—see sheath model 3 in the Supplementary Information) and the *nonPDPSIM* results. The electric field determined from the analytical model considering T_e of 1.8 eV as obtained by the *nonPDPSIM* is also shown (AM— T_e). The vertical dashed grey lines indicate the times when the droplet passes the top and bottom edges of the electrodes.

electron temperature obtained from *nonPDPSIM* in the analytical model (ion continuum model [54]—see sheath model 3 in the Supporting Information), the obtained droplet charge becomes $-1.4 \times 10^5 e$ and is in excellent agreement with the simulation ($-1.1 \times 10^5 e$). This analysis shows that the determination of the droplet charge can be obtained from analytical estimates with reasonable accuracy, and we can estimate an effective electric field from the measured particle force in figure 11(c).

3.6. Electric field determination

With the derived values of the droplet charge from the analytical ion continuum model [54] (see sheath model 3 in the Supporting Information), the electric field responsible for accelerating the droplet can be determined from the known F_{el} using the measured n_e and T_e values. The electric field deduced from the equilibrium of forces is shown in figure 13. The electric fields at the top ($t=0$ ms) and bottom ($t=t_{res}$) edges of the plasma are estimated to be $-1 \times 10^5 V m^{-1}$ and $2 \times 10^5 V m^{-1}$, respectively. These fields are highest at the edges of the plasma where the ambipolar electric fields are the largest and the gradients in plasma densities are the largest. However, these values of electric field underestimate the field calculated using the droplet charge obtained from the *nonPDPSIM* results by a factor of 2.3. Using T_e obtained from the *nonPDPSIM* in the analytical ion continuum model to solve

for the droplet charge, this factor is further reduced to 1.2 leading to better agreement with the simulation results as shown in figure 13.

A remnant field $(-1.0 \pm 0.3) \times 10^4 \text{ V m}^{-1}$ exists in the bulk of the plasma (which is more pronounced for the analytical model due to the higher E-field) for the same reason as the non-zero F_{el} discussed previously. Considering an uncertainty of 25 K in T_{gas} , the uncertainty in the estimated electric field is $1.4 \times 10^4 \text{ V m}^{-1}$, well above the remaining non-zero electric field in the bulk of the plasma. Since ϕ_p depends mainly on T_e (see equation (A8) in the Supporting Information), the electric fields responsible for acceleration of the droplet at the plasma edges were also determined for the range of uncertainties in deriving T_e . A 37% uncertainty in T_e leads to an uncertainty of $\sim 56\%$ in the derived electric fields.

The electric field responsible for F_{el} that accelerates (or decelerates) the droplet at the top and bottom of the plasma likely comes from two sources. The first is the ambipolar electric field that is naturally generated to confine the plasma in the axial direction. The ambipolar electric field (E_{amb}) at the plasma edge can be estimated from [56]:

$$E_{amb} = \frac{D_i - D_e}{\mu_i + \mu_e} \frac{\nabla n}{n}, \quad (7)$$

where D and μ are free diffusion coefficient and mobility, respectively, and the subscripts ‘i’ and ‘e’ represent ions and electrons, respectively. The relative gradient in the electron density, $\nabla n/n$ can be approximated by the local diffusion length in the axial direction, Λ . Since $D_i \ll D_e$ and $\mu_i \ll \mu_e$, the ambipolar field can be estimated using the Einstein relation as [56]:

$$E_{amb} \approx -\frac{k_B T_e}{e} \frac{1}{\Lambda}. \quad (8)$$

For a local electron diffusion length of a few mm, the estimated ambipolar electric field is at most a few tens of V cm^{-1} (a few kV m^{-1}), which is more than an order of magnitude too small to explain the derived F_{el} .

The second origin of the electric field that provides the electrical force responsible likely has contributions from the sheath surrounding the droplet. These principles will be discussed using results for a $40 \mu\text{m}$ diameter droplet. The charge on the droplet and axial electric field surrounding the $40 \mu\text{m}$ diameter droplet predicted by *nonPDPSIM* are shown in figures 12(a) and (b), respectively, for a droplet located at the lower edge of the plasma. The axial electric field largely results from the formation of the sheath around the droplet due to the presence of a net negative charge on the droplet. The electric field is directed towards the droplet, deflecting electrons away from the droplet and attracting positive ions. However, this sheath electric field is not vertically symmetric, as shown in figure 12(c) along the droplet trajectory. The maximum electric field magnitude above the droplet is 4.9 kV cm^{-1} , while the electric field magnitude below the droplet is only 4.3 kV cm^{-1} . This asymmetry in the electric field results from the droplet being in a

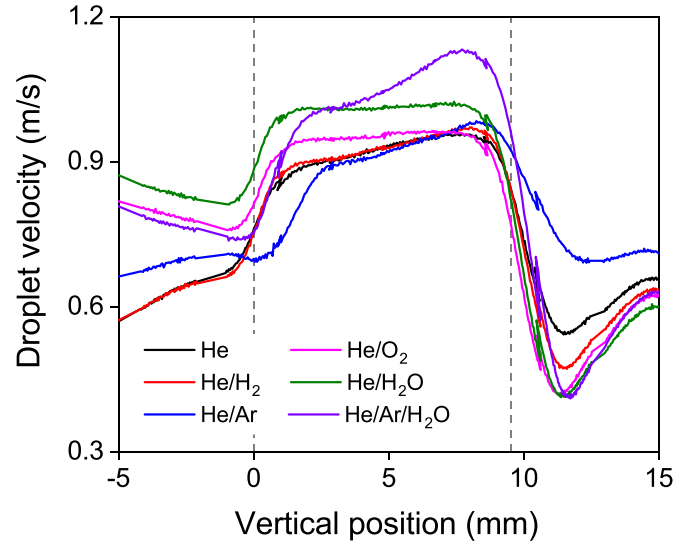


Figure 14. Measured droplet velocity for an initial droplet diameter of $42 \mu\text{m}$ with a total gas flow rate of 1 slm in the presence of plasma in different gas compositions: He (13.6 W), He + 0.2% H_2 (13.6 W), He + 17% Ar (6 W), He + 0.2% O_2 (14.2 W), He + 0.2% H_2O (14.3 W), and He + 17% Ar + 0.2% H_2O (13.4 W). The dashed grey lines indicate the top and bottom edges of the electrode.

gradient of plasma properties at the edge of the plasma. The resulting force on the droplet from the axial electric field above the droplet is then larger than the force from the vertical electric field below the droplet. This force imbalance results in a net force of the order of 1 nN directed upwards, decelerating the droplet as it exits the plasma. This force is commensurate with the experimentally derived force of the order of 7 nN as shown in figure 11(c). The force varies significantly depending on the exact location of the droplet relative to the electrodes as shown in figure 11(c). The degree of axial asymmetry in the sheaths across the droplet is very sensitive to the gradient in the plasma properties at the edge of the plasma, and so is sensitive to the precise location of the droplet (see also figure 11(c)).

3.7. Impact of droplet trajectories on gas composition and plasma power

The sensitivities of the droplet dynamics as a function of gas composition and plasma power are discussed in this section. The droplet velocities in the channel of the reactor from near the dispenser nozzle to 5.5 mm below the bottom edge of the electrode are shown in figure 14 for different gas compositions at a total gas flow rate of 1 slm. Gas admixtures include both electropositive (H_2 , Ar) and electronegative (O_2 , H_2O) gases. In all cases, the droplet is accelerated into the plasma and decelerated during its exit. Since the droplet velocity changes by less than a factor of 2 for these conditions, the variation in F_{el} will be similarly small, consistent with similar T_e and n_e for these gas mixtures as reported in [50]. As a result, there will be a similar charge on the droplet surface and similar ambipolar and sheath electric fields.

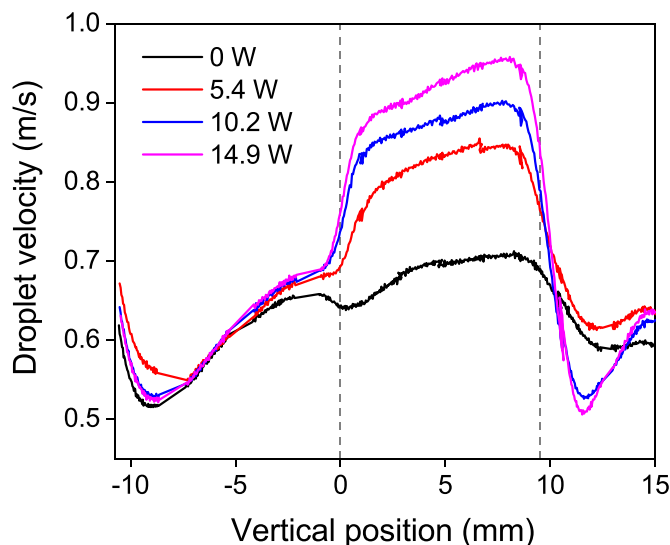


Figure 15. Measured droplet velocity for an initial droplet diameter of $42\ \mu\text{m}$ at different plasma powers and 1 slm He flow. The ‘0 W’ is the no plasma (‘gas only’) case. The dashed grey lines indicate the top and bottom edges of the electrode.

In Ar-containing plasmas, the location of the droplet acceleration is shifted as compared to other plasmas and is highly pronounced in He/Ar plasma. In both He/Ar and He/Ar/H₂O cases, the plasma does not completely fill the inter-electrode volume, and the visible plasma is below the top edge of the electrodes [50]. As such, the locations of plasma gradients responsible for the droplet acceleration are shifted.

With Ar in the gas mixture, the droplet experiences a continuous acceleration that does not produce a steady-state droplet velocity inside the plasma as in the other cases. The increase in the droplet velocity is most likely due to the increased T_{gas} in He/Ar/H₂O plasma in excess of 450 K [50]. This larger gas temperature leads to an increase in the axial temperature gradient and gas velocity, and hence, also the droplet velocity.

The spatial variation in the droplet velocity as a function of the plasma power for a 1.0 slm He flow is shown in figure 15. The droplet acceleration at $z = 0$ and deceleration at $z = 9.5$ mm increases with increasing power, which is due to an increase in F_{el} . As the plasma power increases, n_e increases as shown by Golda *et al* in the case of an RF atmospheric pressure He plasma [57]. Although the droplet potential is not strongly dependent on n_e (see equations (A7) and (A8) in the Supporting Information), the enhanced F_{el} is likely caused by the increase in T_e due to the increased gas heating which also produces steeper gradients in plasma properties. The droplet velocity in the plasma region ($0 < z < 9.5$ mm) also increases with the increase in power in all plasma cases, which might be partially due to the inertia of the droplet enhanced by the initial higher electric field at $z = 0$ mm. Increased gas heating in the plasma region leading to a large temperature gradient will contribute to the observed increase in the droplet velocity and can also account for the faster reduction in the afterglow for larger powers due to the cooling of

the gas. Nonetheless, the larger the plasma power, the greater will be the droplet evaporation further impacting droplet velocity.

4. Conclusions

In this work, we investigated the dynamics of liquid water droplets tens-of-microns in diameter in atmospheric pressure RF glow discharge plasmas by capturing the droplet dynamics using fast framing camera imaging complemented by 2D simulations. The specific case of $42\ \mu\text{m}$ diameter droplets in He plasma at 1 slm and 14 W was chosen to quantitatively describe the droplet transport dynamics. In the absence of plasma, the droplet is entrained in and travels with essentially the speed of the gas flow. The droplet was observed to change speed entering and leaving the plasma, an effect attributed to acceleration in the gradient of electric fields at the edge of the plasma. Using a charge on the droplet derived from experimentally measured plasma parameters, electrical forces of up to 8 nN are required to account for the acceleration, which corresponds to electric fields of $(1 - 2) \times 10^5\ \text{V m}^{-1}$. These electric fields are much larger than the time-averaged ambipolar electric fields at the edge of the plasma. Results from the 2D *nonPDPSIM* model suggest that the charging of the droplet and sheaths bounding the droplet are asymmetric across the diameter of the droplet in the axial direction. The differential charging and sheath electric fields provide a net acceleration that likely explains the observations.

With atmospheric pressure plasma-activated aerosols becoming a more important research area with increasingly important application areas, an outcome of this work is a heightened awareness of the need to globally approach the transport of those droplets. The foundational knowledge for quantifying that transport can be found in studies of dusty plasmas performed under very different conditions. That said, the fundamentals to apply to a broad range of conditions, include atmospheric pressure plasmas. To apply those fundamentals, the focus will need to be on the more unique circumstances not found in the prior studies, such as a collisional sheath, consequences of evaporation, differential charging, and conductivity of the droplets. Using those fundamentals, modified for atmospheric pressure, other opportunities present themselves, potentially opening new pathways for droplet treatment with a highly controlled plasma dose.

Data availability statement

Key data to support findings is provided in manuscript and supplementary information or references provided in data. The raw data files (for example droplet motion video files) are exceedingly large (> 1 GB/file) to be shared and do not add valuable information to support the conclusions and analysis of the work. The data that support the findings of this study are available upon reasonable request from the authors.

Acknowledgments

PJB and GN acknowledge support from the National Science Foundation (PHY 1903151). MJK and MM acknowledge support from the National Science Foundation (No. PHY-1902878), the U.S. Department of Energy, Office of Science, Office of Fusion Energy Sciences under Award No. DE-SC0020232 and the Army Research Office accomplished under Grants Nos. W911NF-20-1-0105 and W911NF-18-1-0240.

Conflict of Interest

The authors have no conflicts of interest to disclose.

ORCID iDs

Gaurav Nayak  <https://orcid.org/0000-0001-5716-0062>
 Mark J Kushner  <https://orcid.org/0000-0001-7437-8573>
 Peter J Bruggeman  <https://orcid.org/0000-0003-3346-7275>

References

- [1] Shukla P K and Eliasson B 2009 *Rev. Mod. Phys.* **81** 25
- [2] Shukla P K and Mamun A 2015 *Introduction to Dusty Plasma Physics* (Boca Raton, FL: CRC Press)
- [3] Thomas H, Morfill G, Demmel V, Goree J, Feuerbacher B and Möhlmann D 1994 *Phys. Rev. Lett.* **73** 652
- [4] Allen J 1992 *Phys. Scr.* **45** 497
- [5] Shotorban B 2011 *Phys. Rev. E* **83** 066403
- [6] Cui C and Goree J 1994 *IEEE Trans. Plasma Sci.* **22** 151–8
- [7] Matsoukas T and Russell M 1995 *J. Appl. Phys.* **77** 4285–92
- [8] Le Picard R and Girshick S L 2016 *J. Phys. D: Appl. Phys.* **49** 095201
- [9] D'yachkov L, Khrapak A, Khrapak S and Morfill G 2007 *Phys. Plasmas* **14** 042102
- [10] Gatti M and Kortshagen U 2008 *Phys. Rev. E* **78** 046402
- [11] Morfill G, Thomas H, Konopka U, Rothermel H, Zuzic M, Ivlev A and Goree J 1999 *Phys. Rev. Lett.* **83** 1598
- [12] Khrapak S et al 2005 *Phys. Rev. E* **72** 016406
- [13] Samsonov D and Goree J 1999 *Phys. Rev. E* **59** 1047
- [14] Tsyтович V, Vladimirov S, Morfill G and Goree J 2001 *Phys. Rev. E* **63** 056609
- [15] Fortov V, Ivlev A, Khrapak S, Khrapak A and Morfill G 2005 *Phys. Rep.* **421** 1–103
- [16] Beckers J, Trienekens D and Kroesen G 2013 *Phys. Rev. E* **88** 055101
- [17] van Minderhout B, Peijnenburg T, Blom P, Vogels J, Kroesen G and Beckers J 2019 *J. Phys. D: Appl. Phys.* **52** 32LT03
- [18] Beckers J, Ockenga T, Wolter M, Stoffels W, Van Dijk J, Kersten H and Kroesen G 2011 *Phys. Rev. Lett.* **106** 115002
- [19] Oinuma G, Nayak G, Du Y and Bruggeman P J 2020 *Plasma Sources Sci. Technol.* **29** 095002
- [20] Toth J R, Abuyazid N H, Lacks D J, Renner J N and Sankaran R M 2020 *ACS Sustainable Chem. Eng.* **8** 14845–54
- [21] Maguire P, Rutherford D, Macias-Montero M, Mahony C, Kelsey C, Tweedie M, Pérez-Martin F, McQuaid H, Diver D and Mariotti D 2017 *Nano Lett.* **17** 1336–43
- [22] Galligani T, Abuyazid N H, Colombo V, Gherardi M and Sankaran R M 2020 *J. Aerosol Sci.* **150** 105631
- [23] Fauchais P, Etchart-Salas R, Rat V, Couderc J F, Caron N and Wittmann-Ténéze K 2008 *J. Therm. Spray Technol.* **17** 31–59
- [24] Fauchais P, Joulia A, Goutier S, Chazelas C, Vardelle M, Vardelle A and Rossignol S 2013 *J. Phys. D: Appl. Phys.* **46** 224015
- [25] Adamovich I et al 2017 *J. Phys. D: Appl. Phys.* **50** 323001
- [26] Taylor G I 1964 *Proc. R. Soc. A* **280** 383–97
- [27] Hunter H C and Ray A K 2009 *Phys. Chem. Chem. Phys.* **11** 6156–65
- [28] Feng X, Bogan M J and Agnes G R 2001 *Anal. Chem.* **73** 4499–507
- [29] Widmann J, Aardahl C and Davis E 1997 *Aerosol Sci. Technol.* **27** 636–48
- [30] Taffin D C, Ward T L and Davis E J 1989 *Langmuir* **5** 376–84
- [31] Doyle A, Moffett D R and Vonnegut B 1964 *J. Colloid Sci.* **19** 136–43
- [32] Hogan Jr C J, Biswas P and Chen D-R 2009 *J. Phys. Chem. B* **113** 970–6
- [33] Seto T, Maekawa T, Osone S, Kawamura K, Yamauchi T and Otani Y 2013 *Chem. Eng. Sci.* **85** 46–49
- [34] Zilch L W, Maze J T, Smith J W, Ewing G E and Jarrold M F 2008 *J. Phys. Chem. A* **112** 13352–63
- [35] Maguire P et al 2015 *Appl. Phys. Lett.* **106** 224101
- [36] Bennet E et al 2016 *J. Aerosol Sci.* **100** 53–60
- [37] Khrapak S and Morfill G 2008 *Phys. Plasmas* **15** 114503
- [38] Nayak G, Simeni Simeni M, Rosato J, Sadeghi N and Bruggeman P 2020 *J. Appl. Phys.* **128** 243302
- [39] Nayak G, Sadeghi N and Bruggeman P 2019 *Plasma Sources Sci. Technol.* **28** 125006
- [40] Schneider C A, Rasband W S and Eliceiri K W 2012 *Nat. Methods* **9** 671–5
- [41] Burm K 2004 *Plasma Sources Sci. Technol.* **13** 387
- [42] Park S, Choe W, Youn Moon S and Park J 2014 *Appl. Phys. Lett.* **104** 084103
- [43] Norberg S A, Johnsen E and Kushner M J 2015 *Plasma Sources Sci. Technol.* **24** 035026
- [44] Van Gaens W and Bogaerts A 2013 *J. Phys. D: Appl. Phys.* **46** 275201
- [45] Norberg S 2015 Modeling atmospheric pressure Plasma jets: plasma dynamics, interaction with dielectric Surfaces, Liquid Layers, and Cells *PhD Thesis* University of Michigan
- [46] Emmert F, Angermann H, Dux R and Langhoff H 1988 *J. Phys. D: Appl. Phys.* **21** 667
- [47] Lietz A M, Barnat E V, Foster J E and Kushner M J 2020 *J. Appl. Phys.* **128** 083301
- [48] Meyer M, Nayak G, Bruggeman P J and Kushner M J 2022 *J. Appl. Phys.* **132** 083303
- [49] Hinds W C 1999 *Aerosol Technology: Properties, Behavior and Measurement of Airborne Particles* (New York: Wiley)
- [50] Nayak G, Oinuma G, Yue Y, Sousa J S and Bruggeman P 2021 *Plasma Sources Sci. Technol.* **30** 115003
- [51] Bruggeman P J, Sadeghi N, Schram D and Linss V 2014 *Plasma Sources Sci. Technol.* **23** 023001
- [52] Brock J R 1962 *J. Colloid Sci.* **17** 768–80
- [53] Shukla P 2001 *Phys. Plasmas* **8** 1791–803
- [54] Patacchini L and Hutchinson I H 2009 *Phys. Plasmas* **16** 062101
- [55] Clements R and Smy P 1974 *J. Phys. D: Appl. Phys.* **7** 551
- [56] Lieberman M A and Lichtenberg A J 2005 *Principles of Plasma Discharges and Materials Processing* (New York: Wiley)
- [57] Golda J, Kogelheide F, Awakowicz P and Schulz-von der Gathen V 2019 *Plasma Sources Sci. Technol.* **28** 095023